Journal of Materials Chemistry A

ROYAL SOCIETY OF CHEMISTRY

PAPER

View Article Online
View Journal | View Issue

Cite this: J. Mater. Chem. A, 2023, 11, 4030

Controlling the density of storable charge of surface faradaic layers on Fe_2O_3 photoanodes for solar rechargeable devices†

Dongjian Jiang,[a] Xiao Sun,[a] Mengfan Xue,[b] Pin Wang,[b] Yingfang Yao,[a] Wenjun Luo *[a] and Zhigang Zou[ab]

Received 30th November 2022
Accepted 22nd January 2023

DOI: 10.1039/d2ta09340e

rsc.li/materials-a

Interface charge transfer plays a key role in a photoelectrochemical cell. Recently, a faradaic junction transfer model was proposed that describes the interface charge transfer process. Electrochemical potential is introduced as a thermodynamic descriptor for the structure and composition of the surface faradaic layer of a semiconductor. However, the kinetic process in the faradaic junction model remains unclear. Herein, we introduce a descriptor, the density of storable charge (DOSC), to describe the number of charges that can be stored in a surface faradaic layer at different applied potentials. Moreover, the DOSC of the faradaic layer on the surface of Fe_2O_3 was modified by Ti doping, and the results suggest that a larger DOSC leads to higher transient photocurrent in a solar rechargeable device, which is helpful for designing other high-performance devices for solar conversion and storage.

Introduction

Photoelectrochemistry has been widely studied over the past few decades for the conversion and storage of solar energy.[1–3] The semiconductor/electrolyte interface plays a key role in the performance of a photoelectrochemical cell.[4–6] Three models have been proposed to understand charge transfer at the semiconductor/electrolyte interface: the direct model, the surface states model, and the faradaic junction model.[6–8] Different from the direct transfer model, the surface states and the faradaic junction models consider photo-generated carriers that are initially trapped by the surface of a semiconductor and then transferred into the electrolyte.[9,10] In the surface states model, no new substance is produced in the surface layer and there is no change in the chemical composition, while a new substance is produced and the chemical composition of the surface layer changes with applied potentials in the faradaic junction model. The composition of a surface faradaic layer depends on potential sensitivity, which can be described by electrochemical potential.[9] However, an electrochemical potential is only a thermodynamic parameter, and the kinetic process in the faradaic junction model remains unclear.

The density of surface states (DOSS), the number of different electronic states allowed to occupy a particular surface energy level, is introduced to quantitatively describe the kinetics process of interface charge transfer in the surface states model. The values are usually measured by electrochemical impedance spectroscopy (EIS),[5,11–13] cyclic voltammetry,[14,15] and chronopotentiometry.[16,17] However, in the faradaic junction model, the carriers are coupled electrons and ions. The rate of ion transfer is much lower than that of electron transfer, which is the rate-determining step during the interface charge transfer. Therefore, the DOSS in the surface states model is not suitable for describing the number of charges (electrons and ions) that can be stored in the surface faradaic layer. To understand the kinetic process of interface charge transfer in a faradaic junction, it is necessary to introduce a parameter to describe the number of charges that can be stored in a surface faradaic layer at different applied potentials.

Herein, we used Fe_2O_3 as a model semiconductor and experimentally determined that the same faradaic reactions occur on the surface of Fe_2O_3 in the dark and under illumination. According to Faraday's law, the product amount of the surface faradaic reaction is proportional to the number of charges through an external circuit. Accordingly, we introduce a descriptor, the density of storable charge (DOSC), to quantitatively describe the number of charges (electrons and ions) that can be stored in the surface faradaic layer at different applied potentials. Moreover, we also modified the DOSC of a Fe_2O_3 semiconductor by Ti doping to investigate the effect of DOSC on the performance of a solar rechargeable device based on a $Fe_2O_3/NiCoO_xH_y$ faradaic junction. The results suggest that a larger DOSC for Fe_2O_3 enables higher transient photocurrent

[a]National Laboratory of Solid State Microstructures, College of Engineering and Applied Sciences, Nanjing University, Nanjing 210093, China. E-mail: wjluo@nju.edu.cn

[b]Eco-materials and Renewable Energy Research Center (ERERC), Jiangsu Key Laboratory for Nano Technology, National Laboratory of Solid State Microstructures and Department of Physics, Nanjing University, Nanjing 210093, China

† Electronic supplementary information (ESI) available. See DOI: https://doi.org/10.1039/d2ta09340e

in the device, which can offer guidance for designing other high-performance solar conversion and storage devices.

Results and discussion

Adjusting the surface composition of a Fe_2O_3 semiconductor by Ti doping

Pristine Fe_2O_3 and Ti-doped hematite (Ti–Fe_2O_3) were prepared on fluorine-doped tin oxide (FTO) by a hydrothermal method at 100 °C for 1 h and annealed at 800 °C for 5 min, following a method from a previous study.[18] Fig. 1a and b shows the surface SEM images of Fe_2O_3 and Ti–Fe_2O_3, respectively. The morphology of Fe_2O_3 and Ti–Fe_2O_3 is that of a rod-like nanostructure, with an average length of 100 nm. XRD and Raman spectra results suggest that the effect of Ti doping on the bulk structure of Fe_2O_3 (Fig. S1†) is negligible. Moreover, the UV-vis spectra of the samples did not obviously change after Ti doping (Fig. S2†). According to previous studies,[19,20] Ti doping can be used to remarkably adjust the surface composition of Fe_2O_3. Therefore, the surface compositions of Fe_2O_3 and Ti–Fe_2O_3 were investigated by XPS, and the results are shown in Fig. 1c–f. Only Fe^{3+} was observed on the surface of Fe_2O_3, while Ti^{4+} and Fe^{3+} were present on the surface of Ti–Fe_2O_3. Moreover, XPS depth analysis (Fig. 1e) indicated that the atomic ratio of Ti to Fe was nearly 1 : 2 on the surface of Ti–Fe_2O_3 and sharply decreased in the bulk, suggesting that Ti^{4+} ions are mainly located on the surface of Ti–Fe_2O_3.

These results are in satisfactory agreement with those of previous studies.[21,22] Moreover, in previous studies, the concentration of surface OH^- played a key role in the charge transfer at the semiconductor/liquid interface.[6,23,24] Therefore, we also used XPS to investigate the change in the surface OH^- of Fe_2O_3 after Ti doping (Fig. 1f). Three characteristic peaks at 529.8 eV, 531.4 eV, and 532.8 eV were assigned to lattice O^{2-}, lattice OH^-, and adsorbed H_2O molecules, respectively.[6,25] By calculating the area of characteristic peaks, the ratio of lattice OH^- to lattice O^{2-} significantly decreased from 0.30 to 0.13 for the surface of Ti–Fe_2O_3 (Fig. S3†). These results suggest that the doping of Ti^{4+} decreases the concentration of lattice OH^- on the surface of Fe_2O_3, which occurs due to the higher activation energy barriers for hydroxylation as well as the reduced adsorption energy of OH^- on the superficial Ti^{4+} sites.[26,27] Therefore, the surface of Fe_2O_3 is covered with hydroxylated $FeO_x(OH)_{3-2x}$, while Ti doping decreases the ratio of lattice OH^-/lattice O^{2-} on the surface of $FeO_x(OH)_{3-2x}$ of Fe_2O_3.

The same faradaic reaction on the surfaces of Fe_2O_3 and Ti–Fe_2O_3 in the dark and under illumination

To investigate the effect of the ratio of lattice OH^-/lattice O^{2-} on the (photo)electrochemical properties of Fe_2O_3, *CV* curves for Fe_2O_3 and Ti–Fe_2O_3 were measured in the dark and under illumination, and the results are shown in Fig. 2a. In the dark, an obvious hysteresis is observed in the *CV* curve for Fe_2O_3, which is related to the redox reaction of $FeO_x(OH)_{3-2x}$ on the surface of electrodes.[28,29] The area of hysteresis remarkably decreased in the *CV* curve for Ti–Fe_2O_3, which is consistent with previous work.[30] Moreover, the electrochemically active surface area of Fe_2O_3 did not change after Ti doping (Fig. S4†). Therefore, the smaller hysteresis comes from the lower amount of surface $FeO_x(OH)_{3-2x}$ of Ti–Fe_2O_3. Under illumination, larger hysteresis and smaller hysteresis were also observed in the *CV* curves for Fe_2O_3 and Ti–Fe_2O_3, respectively. These results suggest that a similar redox reaction occurs on the surface of semiconductors in the dark and under illumination. Although *in situ* FT-IR and Mössbauer spectra have been used to observe high valent state Fe^{4+} at the potentials with hysteresis in previous studies,[31,32] the details of the redox reaction remain unclear.

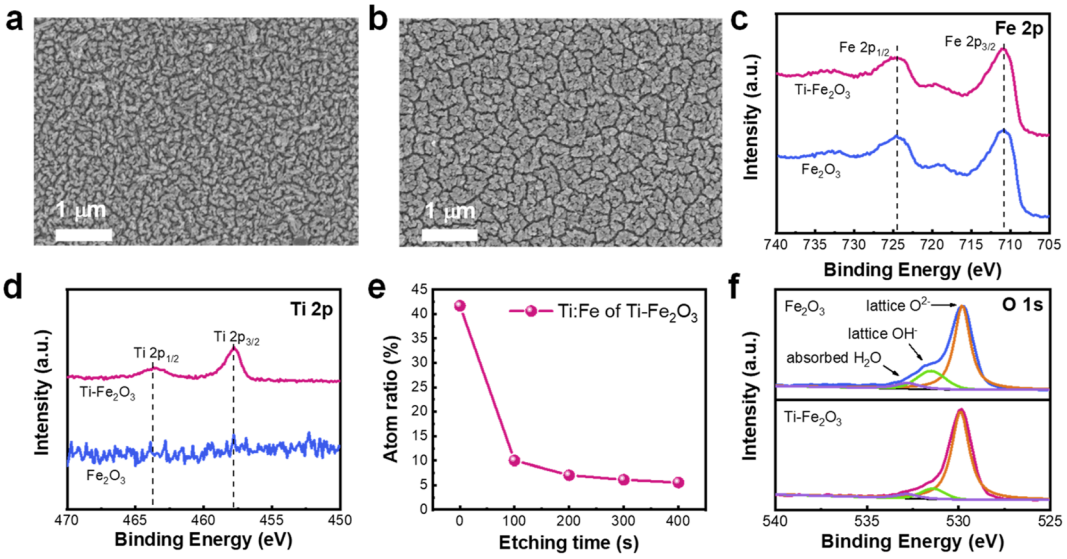

Fig. 1 Surface SEM images of (a) Fe_2O_3 and (b) Ti–Fe_2O_3. XPS spectra of (c) Fe 2p and (d) Ti 2p in Fe_2O_3 and Ti–Fe_2O_3. The atomic ratio of Ti and Fe as a function of etching time obtained from XPS depth analysis of (e) Ti–Fe_2O_3 and (f) XPS spectra of O 1s in Fe_2O_3 and Ti–Fe_2O_3.

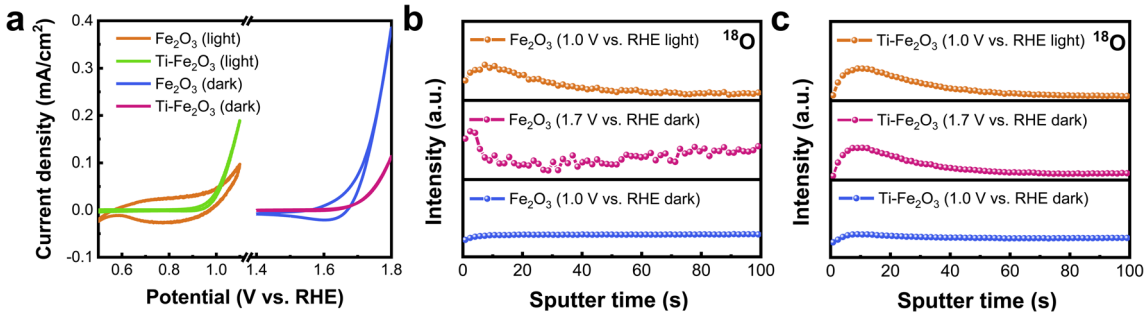

Fig. 2 (a) *CV* curves of Fe_2O_3 and Ti–Fe_2O_3 in the dark and under illumination. TOF-SIMS spectra of ^{18}O depth profile of (b) Fe_2O_3 and (c) Ti–Fe_2O_3 under different conditions. Electrolyte: 1 M KOH, scan rate: 50 mV s^{-1}.

Time-of-flight secondary-ion mass spectrometry (TOF-SIMS) was then used to investigate the interface ion transfer process by ^{18}O isotopic labeling in the electrolyte.[9,33] Fig. 2b and c indicates the ^{18}O depth profiles for Fe_2O_3 and Ti–Fe_2O_3 after *I–t* measurement at different potentials in the dark and under illumination, respectively. Negligible current was observed in Fe_2O_3 at 1.0 V *vs.* RHE in the dark (Fig. S5a†). The intensity of ^{18}O remained unchanged at different depths, and no obvious ^{18}O distribution was observed on the surface of the sample (Fig. 2b). In contrast, ^{18}O was distributed on the surface of Fe_2O_3 after *I–t* measurement at the potential of 1.7 V *vs.* RHE in the dark or at the potential of 1.0 V *vs.* RHE under illumination.

The results suggest that the ^{18}O in the electrolyte diffuse into the surface $FeO_x(OH)_{3-2x}$ on Fe_2O_3 at 1.7 V in the dark or 1.0 V *vs.* RHE under illumination by a faradaic reaction: $Fe^{3+}O_x(OH)_{3-2x} + h^+ + OH^- \leftrightarrow Fe^{4+}O_x(OH)_{4-2x}$. The holes come from FTO in the dark and Fe_2O_3 under illumination, respectively. The same faradaic reaction also occurs on the surface of Ti–Fe_2O_3 after *I–t* measurement at the potential of 1.7 V *vs.* RHE in the dark or at the potential of 1.0 V *vs.* RHE under illumination (Fig. 2c). Therefore, the faradaic reactions on the surfaces of Fe_2O_3 and Ti–Fe_2O_3 are the same in the dark and under illumination, and the smaller hysteresis loop in the *CV* curve of Ti–Fe_2O_3 occurs due to the lower amount of surface $FeO_x(OH)_{3-2x}$ after Ti doping.

The measurement and calculation of DOSC of an intrinsic faradaic layer on a semiconductor surface in the dark

An electrochemical method for double potential step chronoamperometry in the dark was performed according to a previous study,[16] and the results are shown in Fig. 3a and b. From Fig. S6,† the onset potential for the faradaic reaction of the surface faradaic layer is approximately 1.4 V *vs.* RHE. Accordingly, the initial potential of E_1 was set at 1.4 V *vs.* RHE for 10 s (Fig. 3a), and negligible oxidation current was obtained (Fig. 3b). Therefore, there was no faradaic reaction at this potential in the dark. Subsequently, a higher potential of E_2 (1.7 V *vs.* RHE) was applied for an additional 10 s, and an anodic transient current was observed (Fig. 3b) that originated from the oxidation of the surface faradaic layer in the dark.

During the oxidation process, the potential of the surface faradaic layer positively shifted. When the potential was the same as the applied potential of E_2, the anodic transient current disappeared. When the applied potential returned to the initial lower potential of E_1 (Fig. 3a), the oxidized surface faradaic layer was reduced, and the cathodic transient current appeared. After all of the oxidized faradaic layer was reduced, the cathodic current was negligible. Therefore, the amount of oxidized surface faradaic layer (the number of charges stored in the surface faradaic layer) at E_2 (1.7 V *vs.* RHE) can be calculated by integrating the anodic transient current or cathodic transient current (inset in Fig. 3b).

The number of stored charges in the surface faradaic layer on Fe_2O_3 is 468 μC cm^{-2} calculated from the anodic transient current, and 117 μC cm^{-2} calculated from the cathodic transient current (Fig. S7†). Here, the geometric area of the electrode was used to calculate the number of charges that can be stored in the surface faradaic layer because it is difficult to measure the actual area of the nanostructured electrode. The higher value calculated from the anodic transient current is due to the additional current of water oxidation in the anodic current.[15,34] Therefore, the number of stored charges in the surface faradaic layer can be more accurately measured by integrating the cathodic transient current.

Using the same method, the number of stored charges in the surface faradaic layer of Fe_2O_3 and Ti–Fe_2O_3 was measured at different potentials from 1.4 V *vs.* RHE to 1.9 V *vs.* RHE in the dark (Fig. S8†), and the results are shown in Fig. 3c. The number of stored charges in the surface faradaic layer increased at 1.4 V *vs.* RHE and was then saturated at approximately 1.9 V *vs.* RHE. After considering the contribution of double layer charging to the stored charge (Fig. S9†), the maximal number of stored charge for Fe_2O_3 and Ti–Fe_2O_3 was 152 μC cm^{-2} and 12 μC cm^{-2}, respectively. The number of stored charges in the surface faradaic layer of two samples under illumination indicate a value similar to that in the dark (Fig. S10†), which further confirms that the same faradaic reaction occurred under illumination and in the dark. Therefore, the number of stored charges in the surface faradaic layer of Fe_2O_3 decreased to 8% after Ti doping.

Once the numbers of stored charges in the surface faradaic layer of two samples at different potentials are obtained, the DOSC can be calculated by differentiating the number of stored charges with respect to the electrochemical potentials. The

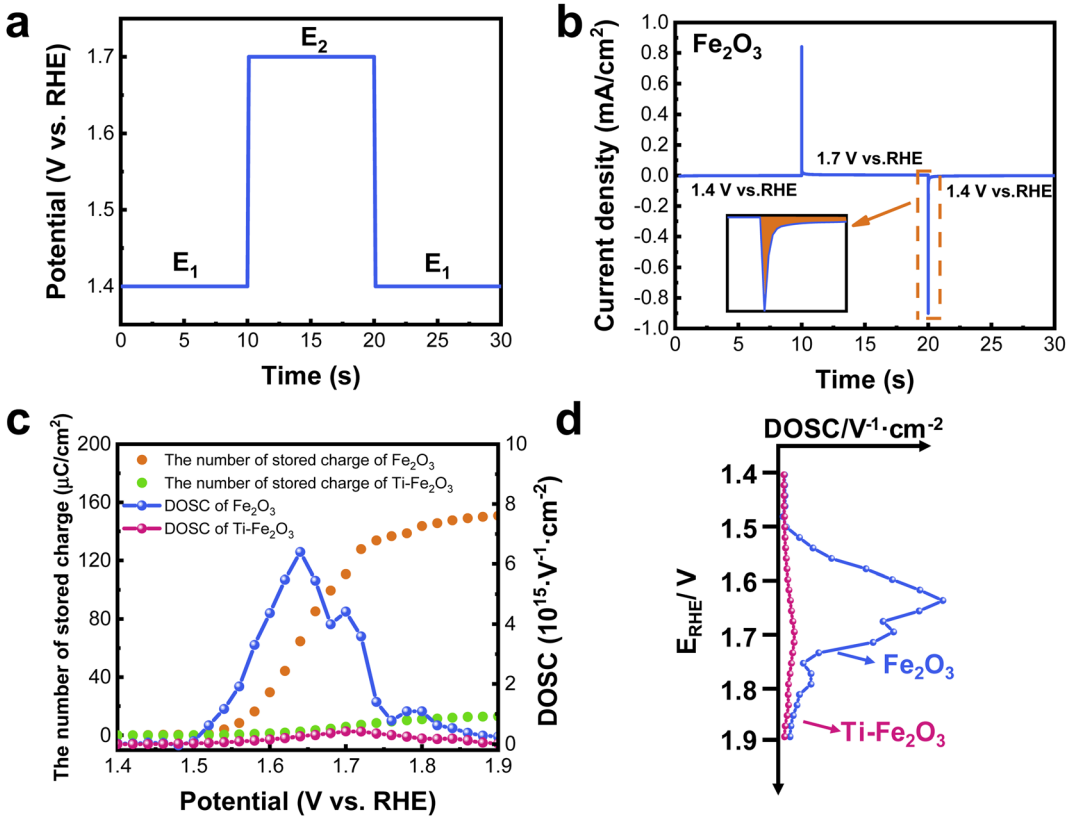

Fig. 3 (a) The pulse of applied potentials, (b) the corresponding current at different applied potentials of Fe_2O_3, and (c) DOSC and the number of charges that can be stored in a surface faradaic layer of Fe_2O_3 and Ti–Fe_2O_3. (d) Schematic diagrams for potential windows of surface faradaic layers for Fe_2O_3 and Ti–Fe_2O_3 in the dark. Electrolyte: 1 M KOH.

DOSC values in the surface faradaic layer of Fe_2O_3 and Ti–Fe_2O_3 are shown in Fig. 3. When the potential is higher than 1.5 V *vs.* RHE, the DOSC of Fe_2O_3 sharply increases, and the maximal value of 6.4×10^{15} V^{-1} cm^{-2} was obtained at approximately 1.65 V *vs.* RHE and then decreased to zero at the potential of 1.9 V *vs.* RHE. Similar to the amount of stored charge, there was a much smaller DOSC for Ti–Fe_2O_3 as compared to Fe_2O_3. The maximal DOSC for Ti–Fe_2O_3 was 4.1×10^{14} V^{-1} cm^{-2} at approximately 1.7 V *vs.* RHE. Like the DOSS in the energy band diagram of surface states of a semiconductor, a graph of DOSC *vs.* applied potential is thus plotted in Fig. 3d.

The effects of DOSC of the surface faradaic layer on the transient photocurrent under illumination

To investigate the effect of DOSC for interface charge transfer kinetics under illumination, *I–t* curves of Fe_2O_3 and Ti–Fe_2O_3 were measured at different applied potentials under chopped light, and the results are shown in Fig. 4 and S11,† respectively. Using 0.8 V *vs.* RHE as an example, in the *I–t* curve for the initial 10 seconds, the current of Fe_2O_3 was negligible in the dark (Fig. 4a). When the light was on, transient photocurrent of 0.18 mA cm^{-2} was observed in Fe_2O_3, which decayed to zero in 3 seconds. When the light was off, a reverse transient dark current of 0.13 mA cm^{-2} appeared, which also decayed to zero in 3 seconds. The *I–t* curve under chopped light is similar to the *I–t* curve with the double potential step method in the dark (Fig. 3b).

The results suggest that the transient photocurrent comes from the faradaic reaction: $Fe^{3+}O_x(OH)_{3-2x} + h^+ + OH^- \leftrightarrow Fe^{4+}O_x(OH)_{4-2x}$ on the surface of Fe_2O_3. To explain the origin of the transient current under illumination and in the dark, the band positions and DOSC of the surface of Fe_2O_3 are illustrated in Fig. 4b and c. In our previous study, when the light was on, reduction and oxidation faradaic layers of TiO_2 were observed on the surface of TiO_2 in photocatalysis.[9] However, in photoelectrocatalysis, only the oxidation of the faradaic layer plays a key role during interface charge transfer when an applied potential is more positive than the potential window of a reduction faradaic layer.

In this study, the applied potential was at 0.8 V *vs.* RHE, which is more positive than the potential window of the reduction faradaic layer of Fe_2O_3 (0.25–0.6 V *vs.* RHE).[9] Therefore, only the oxidation faradaic layer of Fe_2O_3 was plotted in Fig. 4. At the potential of 0.8 V *vs.* RHE, the Fermi level of Fe_2O_3 was adjusted at this applied potential. When Fe_2O_3 was illuminated, 800 mV of photovoltage was measured (Fig. S12†), which led to the quasi-Fermi level of holes at approximately 1.6 V *vs.* RHE.[35] Therefore, the surface faradaic layer is photocharged by $Fe^{3+}O_x(OH)_{3-2x} + h^+ + OH^- \leftrightarrow Fe^{4+}O_x(OH)_{4-2x}$ until the potential of the faradaic layer is equal to the quasi-Fermi

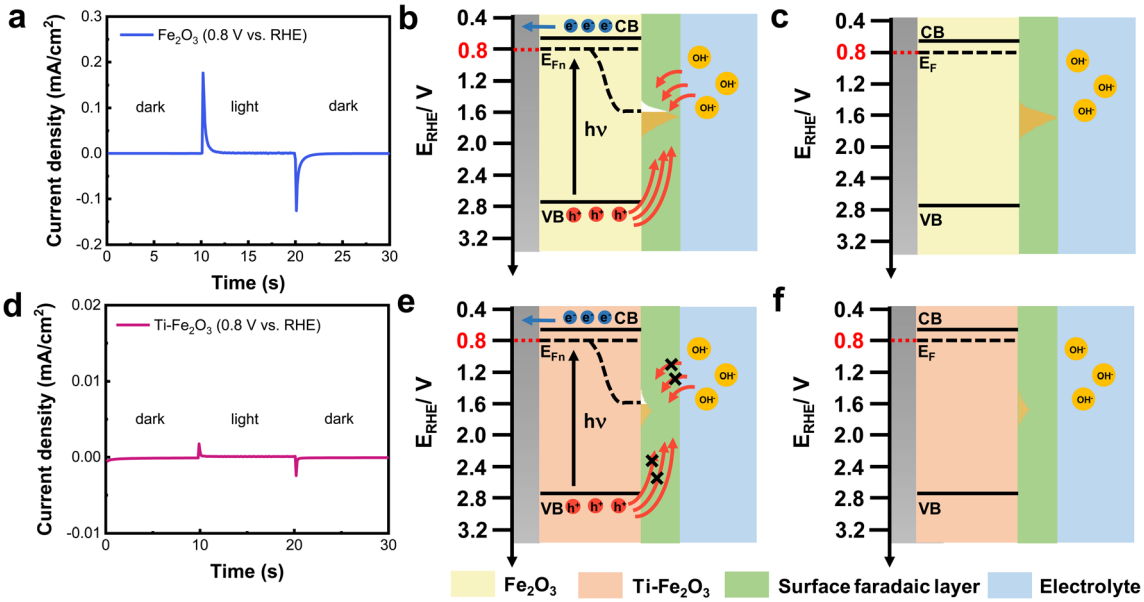

Fig. 4 (a) *I–t* curves of Fe_2O_3 at 0.8 V *vs.* RHE under chopped light. Schematic diagrams for the charge transfer process of Fe_2O_3 (b) under illumination and (c) in the dark. (d) *I–t* curves of Ti–Fe_2O_3 at 0.8 V *vs.* RHE under chopped light. Schematic diagrams for the charge transfer process of Ti–Fe_2O_3 (e) under illumination and (f) in the dark.

level of the holes (Fig. 4b). When the light is off, the partially oxidized faradaic layer is filled with electrons from the substrate and ions from the electrolyte, which leads to reverse transient dark current (Fig. 4c).

The number of charges during dark discharge is the same as that during the photo charge process, which suggests that there is satisfactory reversibility to the faradaic reaction. In contrast, much lower transient photocurrent and dark current were observed in Ti–Fe_2O_3 (Fig. 4d), which resulted from the much smaller DOSC of the faradaic layer (Fig. 4e–f). Therefore, a larger DOSC of the surface faradaic layer leads to higher transient photocurrent and dark current.

Enhanced performance of solar rechargeable devices by controlling the DOSC of a semiconductor surface

In previous studies,[36–38] a higher transient charging photocurrent was used to improve the performance of a solar rechargeable device. Accordingly, Fe_2O_3 and Ti–Fe_2O_3 were used as light absorbers and were coated with $NiCoO_xH_y$ energy storage material and connected with carbon counter electrodes to construct a solar rechargeable device (Fig. 5a). Fig. 5b indicates *I–t* curves of the two devices at zero bias in the dark and under illumination. The $Fe_2O_3/NiCoO_xH_y/KOH_{(aq)}$/carbon device indicates a transient photocurrent of 0.95 mA cm^{-2} when the light is on, which decays to a negligible value within dozens of seconds.

Under illumination, the photo-generated holes, which are initially stored in the surface faradaic layer of Fe_2O_3, subsequently transfer to the $NiCoO_xH_y$ and participate in the faradaic reaction of $NiCoO_xH_y$[39] (Fig. S13†), leading to a higher photocurrent and longer charge time. When the light is off, transient dark current of 0.69 mA cm^{-2} was obtained. In contrast, the Ti–$Fe_2O_3/NiCoO_xH_y/KOH_{(aq)}$/carbon device showed a transient photocurrent of 0.26 mA cm^{-2} and transient dark current of

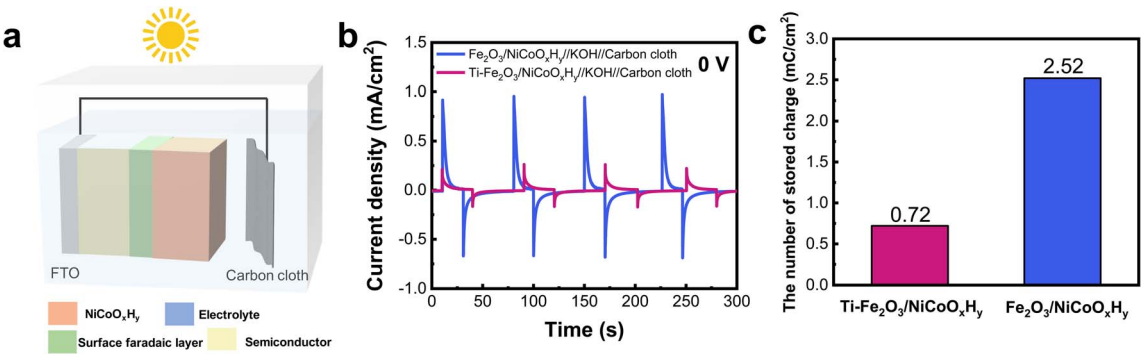

Fig. 5 (a) Configuration of a two-electrode solar rechargeable device. (b) Current–time curves of two devices at zero bias. (c) Charge density of two devices during the photo-charging process.

0.17 mA cm^{-2}, which are both much lower than those for the $Fe_2O_3/NiCoO_xH_y/KOH_{(aq)}$/carbon device. The numbers of stored charges in the two devices were calculated and are indicated in Fig. 5c. The number of stored charges in $Fe_2O_3/NiCoO_xH_y/KOH_{(aq)}$/carbon was 2.52 mC cm^{-2}, which was much higher than the value of 0.72 mC cm^{-2} for Ti–$Fe_2O_3/NiCoO_xH_y/KOH_{(aq)}$/carbon. Moreover, the $Fe_2O_3/NiCoO_xH_y/KOH_{(aq)}$/carbon also exhibited higher photovoltage and satisfactory cycle stability (Fig. S14†).

To exclude the effect of electrodeposited $NiCoO_xH_y$ on the performance of the devices, we characterized the $NiCoO_xH_y$ on Fe_2O_3 and Ti–Fe_2O_3 by inductively coupled plasma mass spectroscopy (ICP), XPS, and Raman methods (Table S1† and Fig. S15†). The results suggest that the loading amount, chemical composition, and crystal structure of $NiCoO_xH_y$ are the same on the two samples. Therefore, the higher performance of the $Fe_2O_3/NiCoO_xH_y/KOH_{(aq)}$/carbon solar rechargeable device is derived from the larger DOSC of the surface faradaic layers on Fe_2O_3.

Conclusions

Electrochemical and TOF-SIMS methods revealed that the same faradaic reactions were observed on the surface of Fe_2O_3 and Ti–Fe_2O_3 semiconductors in the dark and under illumination. To describe the number of charges (electrons and ions) that can be stored in the surface faradaic layer of a semiconductor, the DOSC was introduced and was measured by a double potential step chronoamperometry method. Moreover, the DOSC of the faradaic layer on the Fe_2O_3 surface was modified by Ti doping, which leads to inferior photocharge current for a solar rechargeable device based on a Ti–$Fe_2O_3/NiCoO_xH_y$ faradaic junction. The results suggest that the DOSC is an important parameter for understanding the charge transfer kinetic process in the faradaic junction interface.

Author contributions

W. L. supervised the project, proposed the concept, and designed the experiments. D. J. carried out sample preparation, characterization, and electrochemistry measurements. W. L. and D. J. analyzed the data and wrote the paper. All authors discussed the results and provided comments on the manuscript.

Conflicts of interest

None declared.

Acknowledgements

This work was supported by the National Natural Science Foundation of China (22279052).

References

1 Y. He, T. Hamann and D. Wang, *Chem. Soc. Rev.*, 2019, **48**, 2182–2215.
2 J. Zhang, J. Cui and S. Eslava, *Adv. Energy Mater.*, 2021, **11**, 2003111.
3 Q. Zeng, Y. Lai, L. Jiang, F. Liu, X. Hao, L. Wang and M. A. Green, *Adv. Energy Mater.*, 2020, **10**, 1903930.
4 S. Corby, R. R. Rao, L. Steier and J. R. Durrant, *Nat. Rev. Mater.*, 2021, **6**, 1136–1155.
5 P. Y. Tang, L. J. Han, F. S. Hegner, P. Paciok, M. Biset-Peiró, H. C. Du, X. K. Wei, L. Jin, H. B. Xie, Q. Shi, T. Andreu, M. Lira-Cantú, M. Heggen, R. E. Dunin-Borkowski, N. López, J. R. Galán-Mascarós, J. R. Morante and J. Arbiol, *Adv. Energy Mater.*, 2019, **9**, 1901836.
6 Z. Yin, X. Chen, C. Wang, Z. Guo, X. Wu, Z. Zhao, Y. Yao, W. Luo and Z. Zou, *Chem. Sci.*, 2020, **11**, 6297–6304.
7 Q. Wang and K. Domen, *Chem. Rev.*, 2020, **120**, 919–985.
8 J. Li, W. Wan, C. A. Triana, H. Chen, Y. Zhao, C. K. Mavrokefalos and G. R. Patzke, *Nat. Commun.*, 2021, **12**, 255.
9 M. Xue, Z. Chu, D. Jiang, H. Dong, P. Wang, G. Sun, Y. Yao, W. Luo and Z. Zou, *Natl. Sci. Rev.*, 2022, DOI: **10.1093/nsr/nwac249**.
10 K. George, T. Khachatrjan, M. van Berkel, V. Sinha and A. Bieberle-Hütter, *ACS Catal.*, 2020, **10**, 14649–14660.
11 B. Klahr and T. Hamann, *J. Phys. Chem. C*, 2014, **118**, 10393–10399.
12 B. Klahr, S. Gimenez, F. Fabregat-Santiago, T. Hamann and J. Bisquert, *J. Am. Chem. Soc.*, 2012, **134**, 4294–4302.
13 Q. Shi, S. Murcia-López, P. Tang, C. Flox, J. R. Morante, Z. Bian, H. Wang and T. Andreu, *ACS Catal.*, 2018, **8**, 3331–3342.
14 J. M. Jimenez, G. R. Bourret, T. Berger and K. P. McKenna, *J. Am. Chem. Soc.*, 2016, **138**, 15956–15964.
15 B. Klahr, S. Gimenez, F. Fabregat-Santiago, J. Bisquert and T. W. Hamann, *Energy Environ. Sci.*, 2012, **5**, 7626–7636.
16 H. N. Nong, L. J. Falling, A. Bergmann, M. Klingenhof, H. P. Tran, C. Spori, R. Mom, J. Timoshenko, G. Zichittella, A. Knop-Gericke, S. Piccinin, J. Perez-Ramirez, B. R. Cuenya, R. Schlogl, P. Strasser, D. Teschner and T. E. Jones, *Nature*, 2020, **587**, 408–413.
17 A. L. Roest, J. J. Kelly, D. Vanmaekelbergh and E. A. Meulenkamp, *Phys. Rev. Lett.*, 2002, **89**, 036801.
18 J. W. Jang, C. Du, Y. Ye, Y. Lin, X. Yao, J. Thorne, E. Liu, G. McMahon, J. Zhu, A. Javey, J. Guo and D. Wang, *Nat. Commun.*, 2015, **6**, 7447.
19 D. Monllor-Satoca, M. Bärtsch, C. Fàbrega, A. Genç, S. Reinhard, T. Andreu, J. Arbiol, M. Niederberger and J. R. Morante, *Energy Environ. Sci.*, 2015, **8**, 3242–3254.
20 J. Zhang, Q. Lin, Z. Wang, H. Liu, X. Li and Y. Zhang, *Small Methods*, 2021, **5**, 2100976.
21 D. Cao, W. Luo, J. Feng, X. Zhao, Z. Li and Z. Zou, *Energy Environ. Sci.*, 2014, **7**, 752–759.
22 I. S. Cho, H. S. Han, M. Logar, J. Park and X. Zheng, *Adv. Energy Mater.*, 2016, **6**, 1501840.

23 C. Tang, B. Sun, M. Li, J. Zhang, X. Fan, F. Gao, Y. Tong, L. Dong and Y. Li, *J. Mater. Chem. A*, 2019, **7**, 8050–8054.
24 B. J. Trześniewski, I. A. Digdaya, T. Nagaki, S. Ravishankar, I. Herraiz-Cardona, D. A. Vermaas, A. Longo, S. Gimenez and W. A. Smith, *Energy Environ. Sci.*, 2017, **10**, 1517–1529.
25 W. Luo, C. Jiang, Y. Li, S. A. Shevlin, X. Han, K. Qiu, Y. Cheng, Z. Guo, W. Huang and J. Tang, *J. Mater. Chem. A*, 2017, **5**, 2021–2028.
26 Y. Zhu, Q. Qian, G. Fan, Z. Zhu, X. Wang, Z. Li and Z. Zou, *Chin. Chem. Lett.*, 2018, **29**, 791–794.
27 P. M. Deleuze, H. Magnan, A. Barbier, M. Silly, B. Domenichini and C. Dupont, *J. Phys. Chem. Lett.*, 2021, **12**, 11520–11527.
28 C. Y. Cummings, F. Marken, L. M. Peter, K. G. Wijayantha and A. A. Tahir, *J. Am. Chem. Soc.*, 2012, **134**, 1228–1234.
29 P. Wang, D. Li, H. Chi, Y. Zhao, J. Wang, D. Li, S. Pang, P. Fu, J. Shi and C. Li, *Angew. Chem., Int. Ed.*, 2021, **60**, 6691–6698.
30 O. Zandi, B. M. Klahr and T. W. Hamann, *Energy Environ. Sci.*, 2013, **6**, 634–642.
31 O. Zandi and T. W. Hamann, *Nat. Chem.*, 2016, **8**, 778–783.
32 Z. Kuang, S. Liu, X. Li, M. Wang, X. Ren, J. Ding, R. Ge, W. Zhou, A. I. Rykov, M. T. Sougrati, P.-E. Lippens, Y. Huang and J. Wang, *J. Energy Chem.*, 2021, **57**, 212–218.
33 M. Chen, H. Dong, M. Xue, C. Yang, P. Wang, Y. Yang, H. Zhu, C. Wu, Y. Yao, W. Luo and Z. Zou, *Nat. Commun.*, 2021, **12**, 6363.
34 F. Le Formal, K. Sivula and M. Grätzel, *J. Phys. Chem. C*, 2012, **116**, 26707–26720.
35 X. Chen, K. Zhu, P. Wang, G. Sun, Y. Yao, W. Luo and Z. Zou, *iScience*, 2020, **23**, 100949.
36 P. Wang, X. Chen, G. Sun, C. Wang, J. Luo, L. Yang, J. Lv, Y. Yao, W. Luo and Z. Zou, *Angew. Chem., Int. Ed.*, 2021, **60**, 1390–1395.
37 J. Zhang, D. Jiang, P. Wang, J. Zhong, G. Sun, Y. Yao, W. Luo and Z. Zou, *J. Mater. Chem. A*, 2022, **10**, 1802–1807.
38 P. Wang, M. Xue, D. Jiang, Y. Yang, J. Zhang, H. Dong, G. Sun, Y. Yao, W. Luo and Z. Zou, *Nat. Commun.*, 2022, **13**, 2544.
39 X. Deng, X. Kang, M. Li, K. Xiang, C. Wang, Z. Guo, J. Zhang, X.-Z. Fu and J.-L. Luo, *J. Mater. Chem. A*, 2020, **8**, 1138–1146.